REPORT

MAGNETISM

Direct visualization of magnetic domains and moiré magnetism in twisted 2D magnets

Tiancheng Song[1]†, Qi-Chao Sun[2]†, Eric Anderson[1]†, Chong Wang[3], Jimin Qian[4], Takashi Taniguchi[5], Kenji Watanabe[6], Michael A. McGuire[7], Rainer Stöhr[2,8], Di Xiao[3], Ting Cao[4], Jörg Wrachtrup[2,9]*, Xiaodong Xu[1,4]*

Moiré superlattices of twisted nonmagnetic two-dimensional (2D) materials are highly controllable platforms for the engineering of exotic correlated and topological states. Here, we report emerging magnetic textures in small-angle twisted 2D magnet chromium triiodide (CrI_3). Using single-spin quantum magnetometry, we directly visualized nanoscale magnetic domains and periodic patterns, a signature of moiré magnetism, and measured domain size and magnetization. In twisted bilayer CrI_3, we observed the coexistence of antiferromagnetic (AFM) and ferromagnetic (FM) domains with disorder-like spatial patterns. In twisted double-trilayer CrI_3, AFM and FM domains with periodic patterns appear, which is in good agreement with the calculated spatial magnetic structures that arise from the local stacking-dependent interlayer exchange interactions in CrI_3 moiré superlattices. Our results highlight magnetic moiré superlattices as a platform for exploring nanomagnetism.

The periodic arrangement of atoms in crystals determines their fundamental properties. Modulating the periodicity of a crystal will drastically modify its quantum behavior and may even create new states of matter. An emerging approach along this direction is the creation of moiré superlattices by vertically stacking two layers of van der Waals (vdW) crystals with a small twist angle or a lattice mismatch. This approach has enabled the tailoring of electronic properties of semimetal graphene and semiconducting transition metal dichalcogenides (TMDs), resulting in a series of discoveries of correlated and topological phenomena (*1*–*3*). However, moiré superlattices with intrinsic magnetic order remain challenging to realize experimentally.

The field of two-dimensional (2D) magnets has been growing rapidly over the past few years, and numerous magnets exhibiting different types of magnetic order have been discovered (*4*–*10*). There are several challenges in investigating magnetic moiré superlattices. Most known 2D magnets are very air sensitive, which makes fabrication of moiré superlattice samples technically challenging. The stacking-dependent interlayer magnetic coupling, which is responsible for the moiré effects in vdW magnets, is typically weaker than the magnetic anisotropy and intralayer magnetic exchange interactions, which determine the energy cost of magnetic domain walls. Therefore, the magnetic moiré pattern should exist in small twist-angle samples in which the magnetic domain size is large enough so that the energy gain by forming magnetic domains surpass the energy cost of magnetic domain walls. Because a small twist angle tends to result in lattice reconstruction, the periodic pattern may be substantially disordered, and thus the spatial magnetic structure can be very complicated. Unlike graphene and TMD superlattices, in which the moiré effects on the electronic properties can be probed with transport and far-field optics, moiré effects in magnets mainly manifest in spatially varying magnetic textures (*11*–*13*). Thus, a scanning probe tool with high spatial resolution, sufficient magnetic sensitivity, and low back action of the probe on the sample is needed to investigate spatial magnetic structures in twisted 2D magnets.

We used single-spin quantum magnetometry to investigate twisted 2D magnet chromium triiodide (CrI_3). Recently, scanning magnetometry based on a single electron spin of a nitrogen-vacancy (NV) center in diamond has shown a high spatial resolution of ~50 nm in probing 2D magnets and provides quantitative magnetization information (*14*–*16*). In exploring moiré magnetism, CrI_3 was selected owing to its stacking-dependent interlayer magnetism, as predicted and demonstrated recently (*17*–*22*). In bilayer CrI_3, changing the layer stacking from monoclinic to rhombohedral can switch the sign of interlayer exchange coupling, and thus the magnetic ground state, from antiferromagnetic (AFM) to ferromagnetic (FM), respectively. Furthermore, in a twisted bilayer CrI_3, both monoclinic and rhombohedral stacking regions can emerge (Fig. 1A, blue and red shaded regions), which should lead to the coexistence of AFM and FM domains at the small twist-angle limit (Fig. 1B). Limited by the spatial resolution (~50 nm) of NV center magnetometry, the targeted twist angle of our samples was smaller than ~0.5°. This corresponds to a moiré wavelength above ~80 nm, which is large enough for resolving magnetic structures within and across moiré unit cells.

We began our investigation with a ~0.2° twisted bilayer CrI_3 sample (D1) fabricated by using the "tear and stack" technique (*23*, *24*). Polar reflective magnetic circular dichroism (RMCD) maps at three selected magnetic fields are shown in Fig. 1C, sweeping from 1 T to −0.3 T, which identify monolayer and twisted bilayer areas. Magneto-optical techniques, such as polar RMCD and magneto-optical Kerr effect (MOKE), are sensitive probes of the out-of-plane magnetization (*4*, *25*). All magneto-optical measurements are performed at a temperature of 2 K with out-of-plane magnetic field unless otherwise specified (*23*). The magnetic field–dependent RMCD signal of the twisted bilayer is compared in Fig. 1D with the signals of the nearby monolayer and of a pristine bilayer measured under the same experimental conditions. The monolayer CrI_3 exhibits a single hysteresis loop centered at zero field and sharp spin-flip transitions at ±0.28 T, showing the high quality of the constituent FM monolayers in the twisted bilayer sample. Pristine bilayer CrI_3 with monoclinic stacking behaves as an A-type layered antiferromagnet, showing a vanishing MOKE signal at zero field and spin-flip transitions at around ±0.85 T.

By contrast, the RMCD signal from the twisted bilayer appears to be a mixture of the monolayer and bilayer behaviors. There is a nonzero remanent RMCD signal with a hysteresis loop as a FM monolayer. The spin-flip transition at ±0.85 T is the same as a layered-AFM bilayer. The RMCD map at −0.3 T in Fig. 1C shows this hysteretic mixing effect. The magnetization has already flipped in the monolayer but not yet in the twisted bilayer region, which is consistent with different coercive fields (~0.28 and ~0.85 T, respectively) for the two regions. The difference of the RMCD maps at 1 and 0 T can further identify the twisted bilayer region (Fig. 1C, bottom). These observations imply coexisting AFM and FM domains, likely from the coexistence of monoclinic and rhombohedral layer stacking in twisted

[1]Department of Physics, University of Washington, Seattle, WA 98195, USA. [2]3. Physikalisches Institut, University of Stuttgart, 70569 Stuttgart, Germany. [3]Department of Physics, Carnegie Mellon University, Pittsburgh, PA 15213, USA. [4]Department of Materials Science and Engineering, University of Washington, Seattle, WA 98195, USA. [5]International Center for Materials Nanoarchitectonics, National Institute for Materials Science, 1-1 Namiki, Tsukuba 305-0044, Japan. [6]Research Center for Functional Materials, National Institute for Materials Science, 1-1 Namiki, Tsukuba 305-0044, Japan. [7]Materials Science and Technology Division, Oak Ridge National Laboratory, Oak Ridge, TN 37831, USA. [8]Center for Applied Quantum Technology, University of Stuttgart, 70569 Stuttgart, Germany. [9]Max Planck Institute for Solid State Research, 70569 Stuttgart, Germany.
*Corresponding author. Email: xuxd@uw.edu (X.X.); j.wrachtrup@pi3.uni-stuttgart.de (J.W.)
†These authors contributed equally to the work.

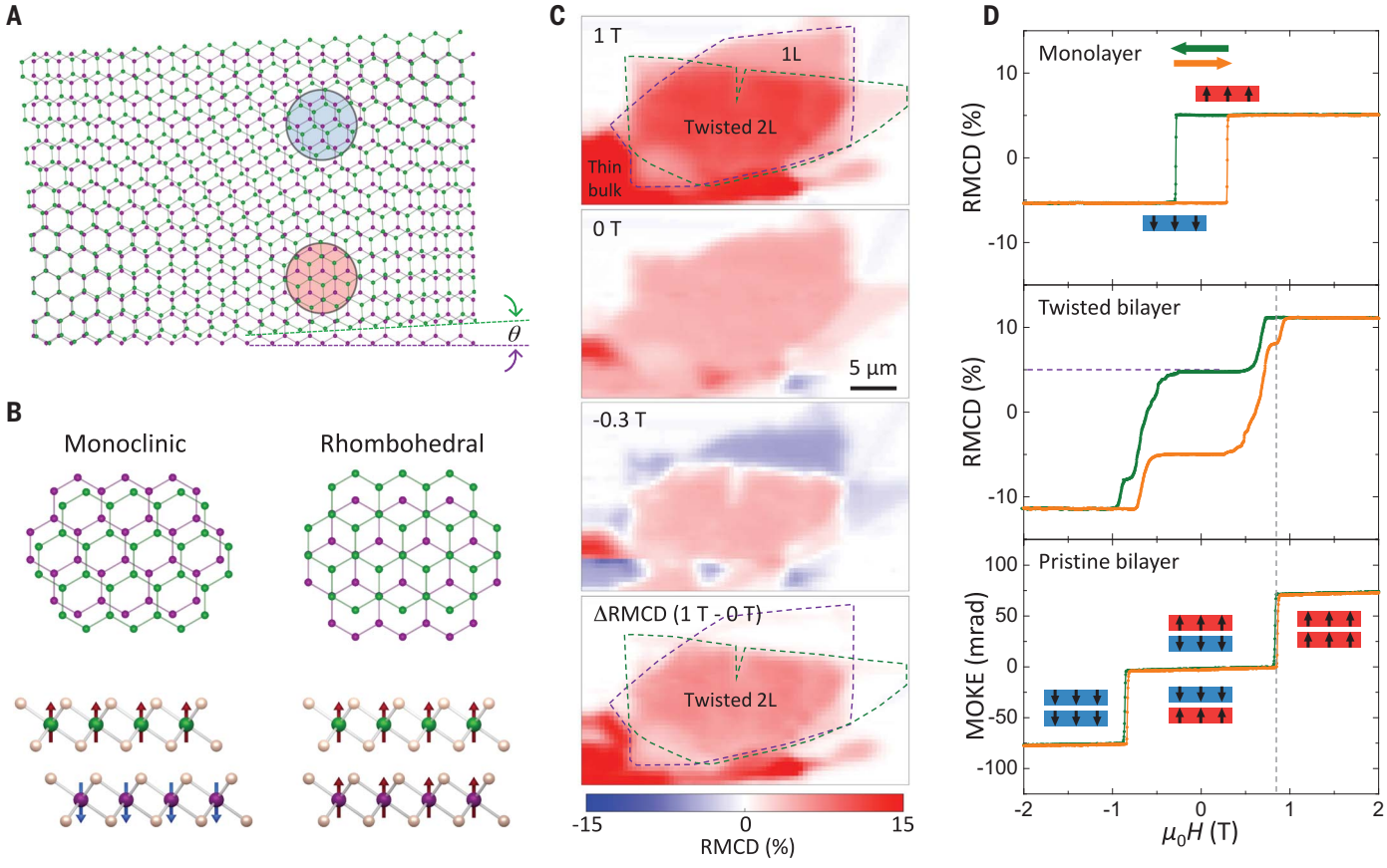

Fig. 1. Layer stacking–dependent magnetism and magneto-optical measurements in twisted bilayer CrI_3. (**A**) Schematic of CrI_3 bilayer with a small twist angle, showing local monoclinic (blue) and rhombohedral (red) stacking. Only Cr atoms appear in the schematic for clarity. Cr atoms in the top and bottom layers are labeled in green and purple, respectively. (**B**) Monoclinic stacking and rhombohedral stacking are associated with the interlayer AFM and FM magnetic states, respectively. (**C**) RMCD maps of the twisted bilayer CrI_3 sample (D1) measured as magnetic field is swept from 1 T, to 0 T, and to −0.3 T. The two monolayer CrI_3 flakes are outlined in green and purple. (Bottom) The difference of the RMCD maps at 1 and 0 T, identifying the twisted bilayer region. (**D**) RMCD and MOKE signals as a function of magnetic field ($\mu_0 H$) for the monolayer, the twisted bilayer, and a pristine bilayer CrI_3. The green and orange curves correspond to decreasing and increasing magnetic field, respectively. (Insets) The corresponding magnetic states.

bilayer CrI_3. In addition, the zero-field RMCD signal of the twisted bilayer is about half of the saturated RMCD signal above 1 T and equivalent to the nearby monolayer signal, which implies a close-to-equal partition between AFM and FM domains. However, owing to the spatial resolution of optical measurements, only homogeneous RMCD maps were observed in the twisted bilayer region. This suggests that the magnetic domain size is much smaller than the laser spot size of ~1 μm.

To access the real-space magnetic textures, we used scanning single NV center spin in a diamond tip (hereafter referred to as magnetometry) with a spatial resolution of ~50 nm to visualize the magnetic domains with quantitative information on the domain magnetization (Fig. 2A) (*14*, *15*). All magnetometry measurements were performed at ~4 K unless otherwise specified (*23*). The RMCD map of the twisted bilayer is shown in Fig. 2B as a reference, with the magnetometry measurement area bounded by the box. By measuring the Zeeman splitting of the NV center spin's energy levels by means of optically detected magnetic resonance, the stray magnetic field emanating from the sample was read out (Fig. 2C). By use of the reverse-propagation protocol, the corresponding out-of-plane magnetization map was reconstructed accordingly (Fig. 2D) (*23*). (the atomic force microscope images measured in situ by using the diamond tip are available in fig. S6).

By contrast to the nearly uniform RMCD map, the magnetometry measurement reveals several fine features. Indicated with the dashed box in Fig. 2B, the twisted bilayer region has a small crack in one of the two monolayers, which is only revealed as a blurred wedge in the RMCD map. In comparison, the stray magnetic field map (Fig. 2C) shows clear imaging of the monolayer region in the crack, which displays an expected uniform magnetization of ~15 Bohr magneton (μ_B)/nm^2 in the magnetization map (Fig. 2D) (*14*). In the twisted bilayer region, domains with high and low stray magnetic fields and magnetization domains were clearly resolved. We could quantify the domains with magnetizations of about 30 and 0 μ_B/nm^2, which unambiguously established the coexistence of FM and AFM domains in twisted bilayer CrI_3.

The emergence of the FM and AFM magnetic domains should originate from the spatial variation of local stacking-dependent interlayer coupling. Shown in Fig. 2, E and F, are magnetization maps at ±0.21 T, which is larger than the coercive fields of monolayer at 4 K. They clearly show that the magnetization in the monolayer region flips, but no change was observed for most of the magnetic domains in the twisted bilayer. The magnetic domain pattern remains the same after multiple thermal and field cycles (fig. S7). These results further support that the magnetic domain pattern originates from the local layer-stacking arrangement, which is fixed once the twisted bilayer is fabricated. The magnetic domain pattern appears disordered, which is consistent across different regions in the same sample and for

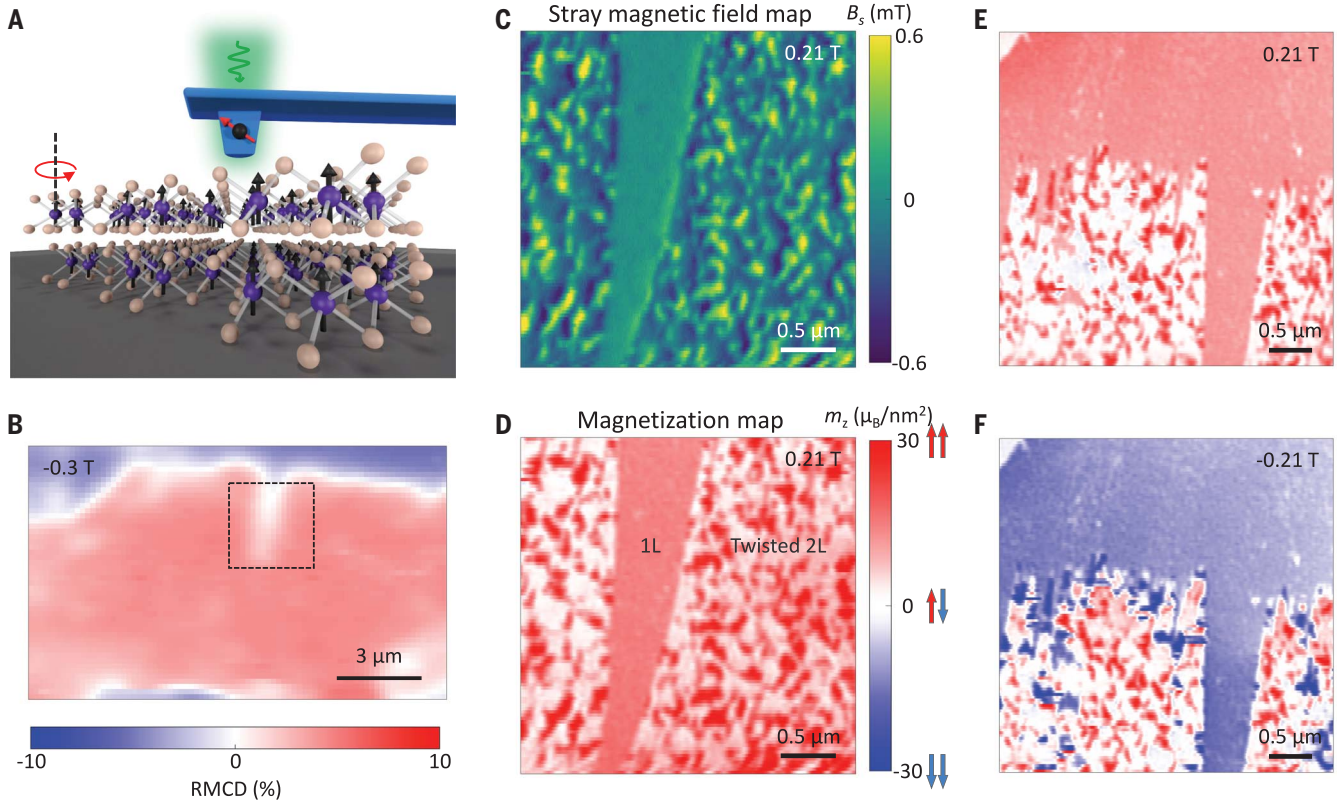

Fig. 2. Scanning NV magnetometry measurements of twisted bilayer CrI_3. (**A**) Schematic of atomic force microscopy with a diamond tip, where the single NV center spin (red arrow) in the tip measures the stray magnetic field emanating from the sample. (**B**) RMCD map of the twisted bilayer region measured at −0.3 T. (**C**) Stray magnetic field map of the dashed box region in (B) with a small crack, measured at 0.21 T. (**D**) Magnetization map at 0.21 T reconstructed from the stray magnetic field map in (C) by using the reverse-propagation protocol (*23*). Nanoscale AFM and FM domains are clearly resolved. The magnetization of monolayer CrI_3 is about ±15 μ_B/nm^2. The schematics of the inferred AFM-FM magnetic states of twisted bilayer are shown along the color bar. (**E** and **F**) Magnetization maps of another area measured at ±0.21 T. The monolayer region undergoes a spin-flip transition, whereas the magnetic domains in the twisted bilayer region remain largely the same between the two maps.

different samples with similar twist angles (figs. S8 and S9).

The lack of a periodic FM-AFM pattern reflects local structural distortion, which could be the result of several factors. The local strain and distortion induced during the fabrication process can disrupt the periodicity of moiré superlattices; this has been observed in transmission electron microscopy images of twisted CrI_3 (*26*, *27*). Compared with twisted heterobilayer, moiré superlattices of twisted homobilayer are more sensitive to local twist-angle variation, leading to more disorder in the periodicity, as has been observed in twisted bilayer graphene (*28*). Furthermore, because we focused on a near-zero twist angle, the area of the moiré unit cell is two orders of magnitude larger than those of magic-angle twisted bilayer graphene and TMD moiré systems and is thus subjected to stronger lattice distortion. CrI_3 is also more fragile and much softer than graphene and TMDs, which can lead to even stronger lattice distortion (*29*). Lattice reconstruction of moiré superlattices is theoretically predicted in twisted CrI_3 for twist angles smaller than 1.3°, at which stacking domains can emerge with stacking domain walls (*13*, *30*–*32*). Additionally, the correspondence between layer stacking and magnetic ground states is nontrivial. Because the interlayer exchange interactions strongly depend on the interlayer atomic registry, the magnetic ground state is highly sensitive to local disorder and is influenced by the competition between adjacent stacking domains (*19*).

Because multilayers are stiffer than monolayers, we next investigated twisted double-multilayer CrI_3 samples—stacking one multilayer on top of another with a small twist angle, with the expectation of reduced lattice reconstruction effects. For the twisted double-bilayer case, the natural interface within the individual bilayer retains AFM coupling, leading to negligible net magnetization in twisted double-bilayer regardless of the stacking arrangement. The twisted double-trilayer case, however, would have nonvanishing magnetization at zero field owing to the one layer of uncompensated magnetization for each individual trilayer. The magneto-optical signal of a small-angle twisted double trilayer is compared in Fig. 3A with a nearby single trilayer and a pristine six-layer sample. The twisted double-trilayer (D2) shows a nonzero remanent MOKE signal with a hysteresis loop, behaving as a trilayer, and intermediate transitions at around ±0.75 T, like a six-layer. Therefore, the twisted double trilayer exhibits a mixture of the trilayer and six-layer properties. These magnetic behaviors also resemble the twisted bilayer case, which arises from a similar coexistence of AFM and FM domains.

The stray magnetic field and reconstructed magnetization maps measured from the double trilayer (D2) with a small twist angle (~0.3°) are shown in Fig. 3, B and C, respectively. The maps confirm the coexistence of AFM and FM domains. Distinct from the disorder-like AFM-FM patterns in twisted bilayer, the mesh patterns in AFM and FM domains seem to have a characteristic length scale of ~150 nm. Because the natural interfaces within the two trilayers retain AFM coupling—either the ↑↓↑ or ↓↑↓ state—the AFM and FM coupled domains should have ↑↓↑↓↑↓ and ↑↓↑↑↓↑ spin arrangements, respectively. Here, arrows indicate the out-of-plane magnetization in individual layers. Therefore, the net magnetization of the FM coupled trilayer should have two layers of uncompensated magnetization. This

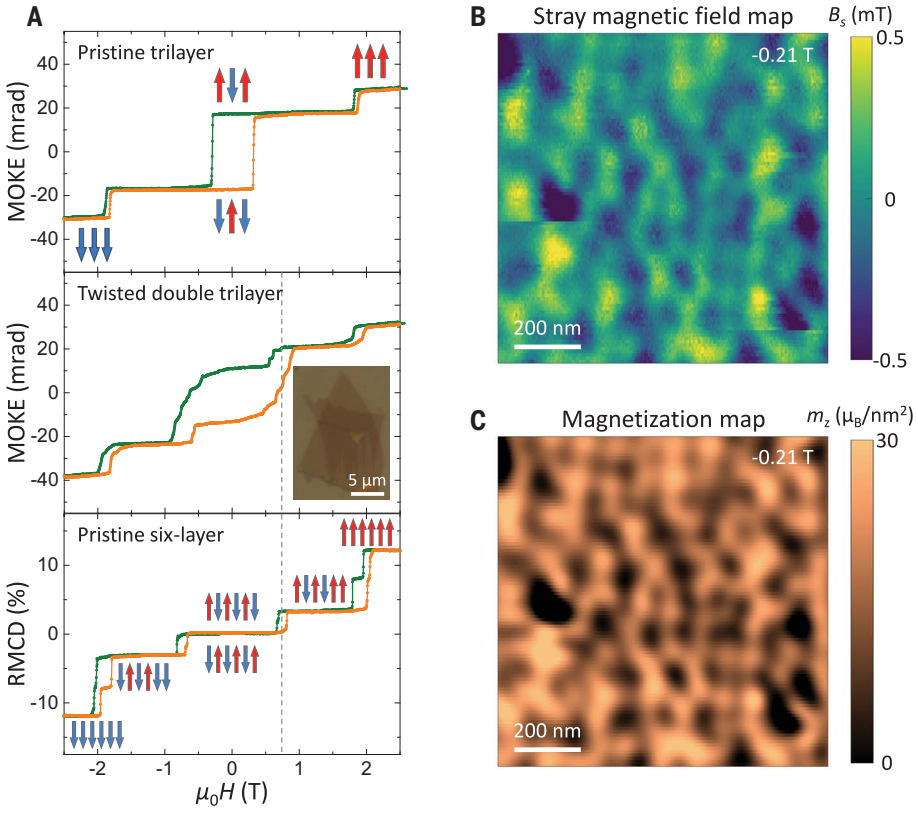

Fig. 3. Magneto-optical and scanning NV magnetometry measurements of twisted double-trilayer CrI_3. (**A**) RMCD and MOKE signals as a function of magnetic field for the trilayer, the twisted double trilayer, and a pristine six-layer CrI_3. (Middle inset) The optical microscope image of the twisted double-trilayer CrI_3 sample (D2). (Insets) The corresponding magnetic states. (**B**) Stray magnetic field map of the twisted double-trilayer region measured at −0.21 T. (**C**) Magnetization map at −0.21 T reconstructed from the stray magnetic field map in (B), showing clear AFM and FM domain structures (*23*).

analysis is consistent with the measured magnetization in these domains, ranging from about 0 to 30 μ_B/nm^2 (Fig. 3C).

We have performed magnetometry measurements on multiple areas. In general, a clear global periodicity in the magnetization map is still obscured by disorder. However, closer inspection of the magnetization maps unveils several micrometer-sized and visibly periodic regions (the fast Fourier transform of the magnetization map is provided in fig. S10, and additional magnetization maps are available in fig. S11). The magnetization map is illustrated in Fig. 4A with a periodic pattern that appears to be hexagonal. For comparison, we investigated a double-trilayer sample with a large twist angle of ~1.2°, which showed uniform magnetization with dominant FM interlayer coupling between the two trilayers (fig. S12). In addition, the atomic force microscope images of all of these samples measured in situ by using the diamond tip (fig. S6) show relatively smooth surfaces. Therefore, the magnetization patterns are unlikely to originate from large-scale segregation caused by trapped hydrocarbons or oxidization between the two CrI_3 layers.

To quantitatively capture the underlying periodicity and symmetry, we calculated the autocorrelation function of the spatially dependent magnetization. Such an approach has been used to reveal periodic magnetic structures obscured by disorder, such as hexagonal magnetic domains with random orientations and densely packed vortices in superconductors (*33*, *34*). The autocorrelation function is defined as

$$AC(\delta x, \delta y) = \sum_{x,y} M(x + \delta x, y + \delta y) M(x, y)$$

where $M(x, y)$ is the magnetization map (*23*). Therefore, $AC(\delta x, \delta y)$ gives the degree of similarity between the map shifted by $(\delta x, \delta y)$ and the original map. It captures the underlying periodic features of a lattice, whereas random features without spatial correlation are averaged out. The normalized autocorrelation of the magnetization map is shown in Fig. 4B, revealing a slightly disordered hexagonal lattice with a lattice constant of ~150 nm and an inferred twist angle of ~0.25°.

The stacking and magnetic structures of small-angle twisted CrI_3 can be calculated, taking into account lattice relaxation (*23*). The calculation for a twisted double-trilayer with a 0.25° twist angle exhibits periodic AFM and FM domains that originate from local monoclinic and rhombohedral stacking domains with out-of-plane magnetization. Possible in-plane magnetization and noncollinear magnetic states can exist in magnetic domain walls with a narrow width (calculated to be less than 5 nm), which can be neglected compared with the domain size. To carry out a direct comparison, we first simulated the stray magnetic field emanating from the predicted magnetic structures on the basis of the distance between the sample and NV center determined in the experiment. The magnetization map was then reconstructed from the simulated stray magnetic field and showed a hexagonal lattice, which is consistent with our experimental observations (Fig. 4C). However, because the measurement spatial resolution is on the order of ~50 nm, sharp features such as the predicted triangular AFM domains and stacking domain walls become blurred in the magnetization map, which prevented us from gaining further information on these features.

The magnetic structure within a moiré unit cell can be extracted from the magnetization map. As shown in Fig. 4D, the autocorrelation, which captures the periodicity and symmetry, was used to identify the moiré superlattice (*23*). We averaged the magnetization over the eight extracted moiré unit cells and obtained the magnetic structure within a moiré unit cell. We observed weak magnetization in the central region of the moiré unit cell, surrounded by higher magnetization, in qualitative agreement with the predicted magnetic structures and simulation results (Fig. 4D, right) (*13*).

We combined magneto-optical measurements and single-spin quantum magnetometry to demonstrate the creation of the coexisting AFM and FM domains in twisted bilayer CrI_3, and show signatures of moiré magnetism in twisted double-trilayer CrI_3. Future studies with improved spatial resolution will reveal details of the magnetic domain pattern, as well as the interplay between lattice reconstruction and the moiré pattern or domain walls. Improved fabrication of NV centers in diamond tips might enhance the spatial resolution of magnetometry to around 20 nm. A combination with structure analysis would unravel the interplay between lattice reconstruction and magnetization patterns. To further improve spatial resolution, techniques such as spin-polarized scanning tunneling microscopy and scanning tunneling spectroscopy can be used, after resolving sample fabrication challenges. Such improvements in spatial resolution would enable the investigation of predicted magnetic phenomena in moiré

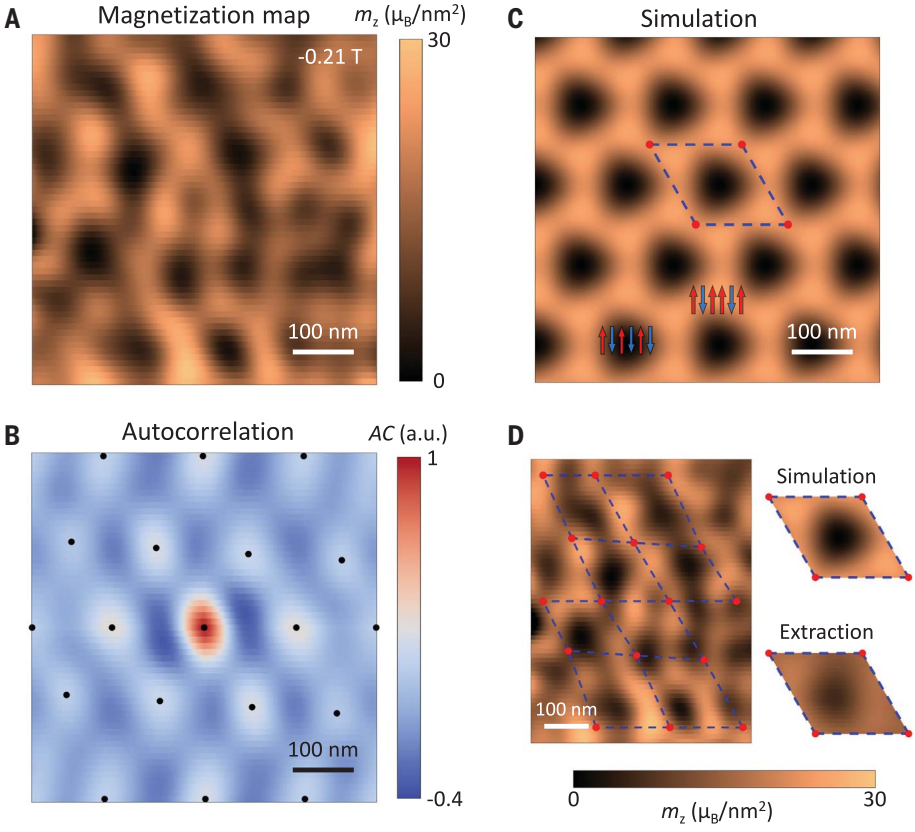

Fig. 4. Moiré magnetic structures of twisted double-trilayer CrI_3. (**A**) Magnetization map revealing a signature of periodicity in hexagonal meshes measured at −0.21 T. (**B**) Normalized autocorrelation map of the magnetization in (A), capturing the periodic hexagonal lattice. The local maxima of the autocorrelation are indicated with black dots. (**C**) Simulation of the reconstructed magnetization map based on the predicted magnetic structures (*23*). (Insets) The corresponding magnetic states. (**D**) (Left) Array of moiré unit cells enclosed by dashed lines. The red dots sit at the same positions as the black dots in the 2D autocorrelation map in (B). (Right) Magnetization structure within a moiré unit cell extracted from the simulation (top) and experimental results (bottom).

magnets, such as moiré skyrmions, noncollinear magnetic states, and one-dimensional magnon channels (*11*–*13*, *35*).

REFERENCES AND NOTES

1. E. Y. Andrei, A. H. MacDonald, *Nat. Mater.* **19**, 1265–1275 (2020).
2. L. Balents, C. R. Dean, D. K. Efetov, A. F. Young, *Nat. Phys.* **16**, 725–733 (2020).
3. D. M. Kennes *et al*., *Nat. Phys.* **17**, 155–163 (2021).
4. B. Huang *et al*., *Nature* **546**, 270–273 (2017).
5. C. Gong *et al*., *Nature* **546**, 265–269 (2017).
6. K. S. Burch, D. Mandrus, J.-G. Park, *Nature* **563**, 47–52 (2018).
7. C. Gong, X. Zhang, *Science* **363**, eaav4450 (2019).
8. K. F. Mak, J. Shan, D. C. Ralph, *Nat. Rev. Phys* **1**, 646–661 (2019).
9. M. Gibertini, M. Koperski, A. F. Morpurgo, K. S. Novoselov, *Nat. Nanotechnol.* **14**, 408–419 (2019).
10. B. Huang *et al*., *Nat. Mater.* **19**, 1276–1289 (2020).
11. K. Hejazi, Z.-X. Luo, L. Balents, *Proc. Natl. Acad. Sci. U.S.A.* **117**, 10721–10726 (2020).
12. Q. Tong, F. Liu, J. Xiao, W. Yao, *Nano Lett.* **18**, 7194–7199 (2018).
13. C. Wang, Y. Gao, H. Lv, X. Xu, D. Xiao, *Phys. Rev. Lett.* **125**, 247201 (2020).
14. L. Thiel *et al*., *Science* **364**, 973–976 (2019).
15. Q.-C. Sun *et al*., *Nat. Commun.* **12**, 1989 (2021).
16. F. Fabre *et al*., *Phys. Rev. Mater.* **5**, 034008 (2021).
17. P. Jiang *et al*., *Phys. Rev. B* **99**, 144401 (2019).
18. D. Soriano, C. Cardoso, J. Fernández-Rossier, *Solid State Commun.* **299**, 113662 (2019).
19. N. Sivadas, S. Okamoto, X. Xu, C. J. Fennie, D. Xiao, *Nano Lett.* **18**, 7658–7664 (2018).
20. S. W. Jang, M. Y. Jeong, H. Yoon, S. Ryee, M. J. Han, *Phys. Rev. Mater.* **3**, 031001 (2019).
21. T. Song *et al*., *Nat. Mater.* **18**, 1298–1302 (2019).
22. T. Li *et al*., *Nat. Mater.* **18**, 1303–1308 (2019).
23. Materials and methods are available as supplementary materials.
24. K. Kim *et al*., *Nano Lett.* **16**, 1989–1995 (2016).
25. T. Song *et al*., *Science* **360**, 1214–1218 (2018).
26. Y. Xu *et al*., arXiv:2103.09850 [cond-mat.mtrl-sci] (2021).
27. H. Xie *et al*, arXiv:2103.13537 [cond-mat.mtrl-sci] (2021).
28. A. Uri *et al*., *Nature* **581**, 47–52 (2020).
29. F. Cantos-Prieto *et al*., *Nano Lett.* **21**, 3379–3385 (2021).
30. H. Yoo *et al*., *Nat. Mater.* **18**, 448–453 (2019).
31. A. Weston *et al*., *Nat. Nanotechnol.* **15**, 592–597 (2020).
32. J. Sung *et al*., *Nat. Nanotechnol.* **15**, 750–754 (2020).
33. P. L. Gammel *et al*., *Phys. Rev. Lett.* **59**, 2592–2595 (1987).
34. P. Reith, X. Renshaw Wang, H. Hilgenkamp, *Rev. Sci. Instrum.* **88**, 123706 (2017).
35. C. Du *et al*., *Science* **357**, 195–198 (2017).
36. T. Song, Replication Data for: Direct visualization of magnetic domains and moiré magnetism in twisted 2D magnets. Harvard Dataverse (2021); doi:10.7910/DVN/CEONCC.

ACKNOWLEDGMENTS

Funding: This work was mainly supported by the US Department of Energy (DOE), Basic Energy Sciences, Materials Sciences and Engineering Division (DE-SC0018171). Theoretical understanding of stacking-dependent interlayer magnetism was partially supported by DOE BES DE-SC0012509. Sample fabrication and magneto-optical measurements were partially supported by the Air Force Office of Scientific Research (AFOSR) Multidisciplinary University Research Initiative (MURI) program, grant FA9550-19-1-0390. The computational imaging analysis was partially supported by NSF MRSEC DMR-1719797. T.C. acknowledges support from the Micron Foundation. M.A.M. was supported by the DOE, Office of Science, Basic Energy Sciences, Materials Sciences and Engineering Division. K.W. and T.T. acknowledge support from the Elemental Strategy Initiative conducted by the MEXT, Japan, grant JPMXP0112101001, JSPS KAKENHI grant JP20H00354, and the CREST (JPMJCR15F3), JST. X.X. acknowledges support from the state of Washington–funded Clean Energy Institute and the Boeing Distinguished Professorship in Physics. J.W. acknowledges funding by the EU through ASTERIQS, European Research Council through ERC grant 742610, SMeI, the DFG through GRK 2642 and FOR 2724, and the BW Foundation through project SPOC. **Author contributions:** X.X., T.S., J.W., and Q.-C.S. conceived the experiment. T.S. fabricated the samples. T.S. and E.A. performed the magneto-optical measurements. Q.-C.S. performed the scanning NV magnetometry measurements, assisted by T.S. and R.S.. C.W. and D.X. calculated the moiré structures and magnetization patterns. J.Q. and T.C. performed the autocorrelation calculations and the extraction of moiré magnetic structures, assisted by E.A. and T.S.; T.S., Q.-C.S., E.A., D.X., T.C., J.W., and X.X. analyzed and interpreted the results. T.T. and K.W. synthesized the hBN crystals. M.A.M. synthesized and characterized the bulk CrI_3 crystals. T.S., Q.-C.S., E.A., J.W., and X.X. wrote the paper, with inputs from all the authors. All the authors discussed the results. **Competing interests:** The authors declare that they have no competing interests. **Data availability:** All data shown in the main text and supplementary materials are available in the Harvard Dataverse repository (*36*).

SUPPLEMENTARY MATERIALS

science.org/doi/10.1126/science.abj7478
Materials and Methods
Supplementary Text
Figs. S1 to S12
References (*37*–*45*)

29 May 2021; accepted 2 October 2021
10.1126/science.abj7478